NASA TM X-221

NASA TM X-1

TECHNICAL MEMORANDUM

HEAT-TRANSFER AND PRESSURE MEASUREMENTS ON A CONCAVE-NOSE CYLINDER FOR A MACH NUMBER RANGE OF 2.49 TO 4.44

By Robert L. Stallings, Jr., and Paige B. Burbank

Langley Research Center
Langley Field, Va.

NATIONAL AERONAUTICS AND SPACE ADMINISTRATION
WASHINGTON
October 1959

NATIONAL AERONAUTICS AND SPACE ADMINISTRATION

TECHNICAL MEMORANDUM X-221

HEAT-TRANSFER AND PRESSURE MEASUREMENTS ON A CONCAVE-NOSE CYLINDER FOR A MACH NUMBER RANGE OF 2.49 TO 4.44*

By Robert L. Stallings, Jr., and Paige B. Burbank

SUMMARY

Heat-transfer coefficients and local pressures were obtained on a 5.46-inch-diameter cylinder with a concave nose in the Langley Unitary Plan wind tunnel for a Mach number range from 2.49 to 4.44, Reynolds number range from 0.94×10^6 to 2.16×10^6, and angle-of-attack range from 0° to 15°.

Two types of flow phenomena were associated with this investigation: a steady-flow condition and a nonpredictable, sporadic, unsteady-flow condition similar to inlet buzzing. During steady-flow conditions the local pressures from the stagnation point to approximately 80 percent of the concave-nose surface length corresponded to the total pressure behind a normal shock throughout the Mach number and angle-of-attack ranges. The stagnation heat-transfer coefficients on the concave nose were 20 percent of those for a hemisphere under steady-flow conditions and increased by a factor of 6 for unsteady-flow conditions. During steady-flow conditions the total convective heat input for a constant temperature potential was approximately the same for the concave nose and a flat-face nose - 70 percent of the value for a convex hemispherical nose.

INTRODUCTION

Various degrees of nose blunting have been used to alleviate the high heat-transfer rates in the stagnation region of hypersonic missiles. Theoretical calculations and experimental data have proved that the stagnation heat transfer is a function of the local velocity gradient and can be reduced by increasing the degree of bluntness. For example, the stagnation heat-transfer coefficient measured on a flat face at $M = 2.49$ and 3.57 as presented in reference 1 was 55 percent of the theoretical heat-transfer coefficient on a hemisphere.

*Title, Unclassified.

Preliminary tests conducted on a concave nose (refs. 2 and 3) indicated that the stagnation heat-transfer coefficient, for steady-flow conditions, was 20 to 40 percent of that for a hemisphere. However, as discussed in reference 3, at zero and small angles of attack an intermittent unsteady flow similar to inlet buzzing existed, which resulted in a large increase in the heat-transfer coefficients on the front face. Tests were conducted in the Langley Unitary Plan wind tunnel to determine the effect of Mach numbers from 2.49 to 4.44, Reynolds numbers from 0.94×10^6 to 2.16×10^6, and angles of attack from 0° to 15° on the distribution of heat-transfer coefficients on a concave nose and to determine the flow stability from high-speed schlieren movies. The tunnel size permits the translation of large models with detailed instrumentation through a range of α.

SYMBOLS

A	area, sq ft
A_s	percent of nose-surface area, measured from axis of symmetry
b	skin thickness, in.
c_w	specific heat of model skin, Btu/(lb)($^\circ$R)
D	model diameter, ft
h	heat-transfer coefficient, Btu/(sec)(sq ft)($^\circ$R)
M	free-stream Mach number
ΔM	variation in free-stream Mach number
p	pressure, lb/sq ft
r	nose radius, ft
r_t	model afterbody radius, ft
R	Reynolds number based on model diameter, $\frac{\rho_\infty U_\infty D}{\mu_\infty}$
S	distance along surface from stagnation point, ft (fig. 2)
S_1	distance along surface from stagnation point to lip, 0.33 ft (fig. 2)

t	time, sec
T	temperature, $^{\circ}R$
T_e	effective air temperature at wall (some temperature which gives a thermal potential that is independent of heat-transfer coefficient), $^{\circ}R$
U	velocity, ft/sec
w	specific weight of wall material, lb/sq ft
α	angle of attack, deg
ρ	density of air, slugs/cu ft
μ	dynamic viscosity of air, slugs/(ft)(sec)

Subscripts:

l	local conditions outside boundary layer
w	wall conditions
t	stagnation
2	conditions behind normal shock
∞	free stream
n	time greater than zero
0	zero time

MODEL AND INSTRUMENTATION

The heat-transfer coefficients and pressures were measured on the model shown in figure 1, but the flared afterbody was not used in these tests. The model was spun from a 0.050-inch sheet of Inconel. The concave nose had sufficient structural rigidity to withstand the airloads, thereby eliminating the necessity of a backing material. The model interior was vented to free-stream static pressure to minimize internal convection losses. The model was instrumented with 15 iron-constantan thermocouples spot-welded to the inner skin surface and eleven 0.050-inch (inside diameter) pressure orifices. The thermocouple and pressure-orifice locations and the model dimensions are shown in figure 2.

APPARATUS AND TESTS

The tests were conducted in the high Mach number test section of the Langley Unitary Plan wind tunnel. This variable-pressure continuous-flow tunnel has an asymmetrical sliding-block nozzle that permits a continuous variation in the test section Mach number from 2.3 to 4.65 and is described in reference 4.

The test conditions were as follows:

M	ΔM	Pressure tests		Heat-transfer tests	
		R	α, deg	R	α, deg
2.49	±0.01	1.15×10^6	0 to ±15	1.01×10^6	0 to ±15
3.51	±.03	1.18	0 to ±15	.94 1.74	0 to ±15
4.44	±.04	1.13	0 to ±15	2.16	0

The model was moved through a positive and negative α range to define the complete heat-transfer and pressure distribution over the front face and sides.

The test technique is the same as that discussed in reference 5. The pressures were measured on manometer boards using a bromoethylbenzene fluid and were photographically recorded.

DATA REDUCTION

Pressure Tests

The local pressures on the model were reduced to the nondimensional ratios $\frac{p_l}{p_{t,2}}$, where $p_{t,2}$ was measured by an orifice at the center of the concave nose with the model at $\alpha = 0^\circ$.

Heat-Transfer Tests

The heat-transfer coefficients were obtained from transient skin-temperature measurements resulting from a stepwise increase in stagnation temperature as shown in reference 5. The following relation, which assumes constant temperature through the skin, negligible lateral heat flow, negligible heat flow to the model interior, and no losses due to radiation, was used:

$$h = \frac{wc_w \frac{dT_w}{dt}}{T_e - T_w}$$

This equation is written in the following form for complete machine tabulation:

$$h = \frac{wc_w\left(T_{w,n} - T_{w,0}\right)}{\frac{T_e}{T_t}\sum_{t=0}^{t=n} T_t - \sum_{t=0}^{t=n} T_w}$$

Here the summations are evaluated over increments of time according to the trapezoidal rule and the ratio T_e/T_t is experimentally determined.

RESULTS AND DISCUSSIONS

Flow Visualization

There are two types of flow associated with this investigation, steady and unsteady. Visual observation with a schlieren system indicated that a nonpredictable, sporadic, unsteady-flow condition occurred throughout the Mach number range. The unsteady flow, similar to inlet buzzing, was an intermittent condition more predominant at small angles of attack and higher Mach numbers. At Mach numbers of 2.49 and 3.51 and an angle of attack of 7.5°, the flow instability still occurred but the time interval between the buzz conditions had greatly increased. At these Mach numbers and an angle of attack of 15° the flow was completely stable with time. At $M = 4.44$ the flow was unstable throughout the angle-of-attack range. A high-speed movie camera (2,000 frames per second) was utilized to determine the nature of the bow-shock oscillation

during the unsteady-flow condition. In figure 3, two sections of the high-speed film are presented to illustrate the oscillating bow shock at $M = 4.44$ and $\alpha = 2^{\circ}$. The first sequence of pictures, frames 1 to 12, depict the flow conversion from steady to unsteady, and in the second sequence, frames 13 to 24, the flow converts back to a steady condition. The high frequency of the bow-shock oscillation is indicated by the shock locations in adjacent frames. The time interval for each sequence of 12 pictures was approximately 0.006 second.

Pressures

The pressure ratios $\frac{p_l}{p_{t,2}}$ over the front face and sides of the model at $\alpha = 0^{\circ}$ are presented in figure 4 for Mach numbers of 2.49, 3.51, and 4.44. The local pressures from the center of the front face to approximately 80 percent of the concave-nose surface length corresponded to the total pressure behind a normal shock throughout the test Mach number range. The only significant Mach number effect occurred at the lip, where $\frac{p_l}{p_{t,2}}$ increased with an increase in Mach number. Increasing the Mach number from 2.49 to 3.51 resulted in a 12-percent increase in $\frac{p_l}{p_{t,2}}$, and increasing the Mach number from 2.49 to 4.44 resulted in a 52-percent increase. There was no significant effect of Mach number on the instrumented portion of the cylindrical side, which apparently was within the region of flow separation originating at the lip.

The pressure ratios are presented in figure 5 for a Mach number of 4.44 and α values from 0° to 15°. The local pressures correspond to the total pressure behind a normal shock from the center of the front face to approximately 80 percent of the concave-nose surface length for the entire α range, excluding the leeward side at $\alpha = 2^{\circ}$. The leeward pressure distribution at $\alpha = 2^{\circ}$ was recorded during unstable flow and the rapid oscillation of pressure with time (discussed in ref. 3) indicates that the measured magnitudes are not reliable. When the pressure distribution was obtained for the windward side at $\alpha = 2^{\circ}$ the flow had returned to a stable condition. Since the heat transfer at the stagnation point is proportional to the local velocity gradient, the constant pressure and corresponding velocity distribution across the cup indicates the low heat transfer that will occur during steady-flow conditions. The behavior of the pressures on the cylindrical sides, where $\frac{S}{S_1} > 1$, is very similar to that on a flat-face cylinder at the same test conditions. (See ref. 1.) The pressure orifices on the leeward side of the

model are located in the separated-flow region originating at the lip and remain approximately constant throughout the α range. The unstable-flow effects occurring on the front face at $\alpha = 2^{\circ}$ are not apparent over this region.

Heat Transfer

Typical time histories of the temperature at the stagnation point on the concave nose during stable and unstable flow conditions are shown in figure 6 for $M = 2.49$. These histories are presented at different angles of attack. However, for steady-flow conditions in the vicinity of the stagnation point, the effect of angle of attack on the heat transfer is negligible. As shown in the figure, the slope of the curve for the unsteady-flow condition is much larger than that for a steady-flow condition. The time interval used for evaluations of the integrals in the heat-transfer equation is also shown in this figure.

Figure 7 illustrates the distribution of heat-transfer coefficients on the concave-nose model at zero angle of attack throughout the Mach number range of the investigation. For comparison the hemispherical stagnation heat-transfer coefficient for $M = 3.51$ and $R = 0.96 \times 10^6$, computed from a modification of Sibulkin's equation as discussed in reference 1, is also presented in figure 7. The extremely high heat-transfer coefficients over the concave face associated with the unstable-flow phenomenon are shown for a Mach number of 4.44 and Reynolds number of 2.16×10^6. The unsteady-flow heat-transfer coefficient at the center of the face was approximately six times the experimental steady-flow value at a Mach number of 2.49 and was of approximately the same magnitude as the hemispherical stagnation value. There is an increase in heat-transfer coefficient with an increase of Reynolds number, but the magnitude of this effect at the stagnation point is much less than the unsteady-flow effects. The small temperature-time differentials on the instrumented portion of the cylindrical side during the unsteady-flow condition were within the accuracy of the recording equipment and are not presented.

The effect of increasing the Mach number from 2.49 to 3.51 during steady-flow conditions is also shown in figure 7. The Mach number effect on the heat-transfer coefficients was small between the stagnation point and $\frac{S}{S_1} = 0.66$. A decrease in h with increase in Mach number was noted, however, between station 0.66 and the model lip, the value at the lip being approximately 20 percent less at the higher Mach number. The readings obtained from the single thermocouple on the lip of the concave nose were converted to heat-transfer coefficients by using an equivalent skin thickness obtained by dividing the element of skin volume by its

external surface area. The high temperature gradient in the vicinity of the lip results in conduction losses to the regions of lower heating around the cylindrical afterbody and inside the concave nose. These conduction losses were not considered in calculating the heat-transfer coefficients.

The absence of instrumentation prevents definite conclusions pertaining to the h distribution along the cylindrical sides beyond $\frac{S}{S_1} = 1.8$. The rapid increase of the heat-transfer coefficients with surface length for S/S_1 values greater than 1.4 is similar to the h distribution associated with boundary-layer transition from laminar to turbulent on the sides of a flat-face cylinder (ref. 1).

The effect of increasing the Reynolds number from 0.94×10^6 to 1.74×10^6 at a Mach number of 3.51 and zero angle of attack is presented in figure 8. The increase in Reynolds number caused a general increase in h over the front face, amounting to approximately 55 percent. The high heating of the cylinder sides is believed to be associated with a boundary-layer transition from laminar to turbulent.

The effect of angle of attack on the heat-transfer coefficients over the front face and sides of the model is presented in figure 9 for a Mach number of 2.49. The heat-transfer coefficients measured at zero angle of attack on the windward side are also plotted in corresponding positions on the leeward side, on the assumption that the flow field is symmetrical. The heat-transfer measurements indicate that steady flow existed throughout the angle-of-attack range except on the leeward side at $\alpha = 7.5^\circ$. Under steady-flow conditions the effect of angle of attack was most noticeable in the vicinity of the model lip. Increasing the angle of attack from 0° to 7.5° resulted in a 16-percent increase of the heat-transfer coefficient at the windward station $\frac{S}{S_1} = 0.95$; increasing α from 0° to 15° resulted in a 27-percent increase. Increasing the angle of attack from 0° to 15° decreased h by 20 percent at the leeward station $\frac{S}{S_1} = 0.947$. The high heat-transfer coefficients on the front face for $\alpha = 7.5^\circ$ obviously resulted from an unsteady-flow condition which produced a stagnation value approximately six times the steady-flow value at $\alpha = 0^\circ$.

In figure 10 the heat-transfer parameter $h\sqrt{D}$ and the percentage of the nose surface area from the stagnation point are plotted for the concave-nose configuration and for a hemisphere and a flat face under steady-flow conditions at $M = 3.51$, $R = 1.8 \times 10^6$, and $\alpha = 0^\circ$. The hemispherical heat-transfer coefficients were calculated by the theoretical method of Lester Lees (ref. 6). This method is not limited by an isothermal

adiabatic wall-temperature distribution. The concave-nose values were from the present investigation; the flat-face values were obtained from reference 1. As shown in the figure the stagnation heat-transfer coefficient of the flat-face body is approximately 55 percent of that for a hemisphere of the same diameter, and the concave-nose stagnation value is only 20 percent of the hemisphere stagnation value. Hence, if low heat-transfer rates at the stagnation point are mandatory for a body of a given diameter, the concave nose would be the desirable configuration provided a steady flow could be maintained. However, if the governing criterion is a body of a given diameter with the lowest total heat input to the front face, consideration must be given to the fact that the heating on the concave nose from $\frac{r}{r_t} = 0.8$ to $\frac{r}{r_t} = 1.0$ is acting on approximately 60 percent of its frontal surface area.

The total convective heat input to a body is proportional to the summation of hA, the local area-weighted heat-transfer coefficients, over the body. These local coefficients are the products of the local heat-transfer coefficients and the differential areas on which they act. This summation for the concave nose is presented in figure 11 for the same free-stream conditions as those in figure 10. The ordinate scale is the summation of the area-weighted heat-transfer coefficients from the stagnation point and the abscissa scale is the ratio of the integrated nose-surface area from the stagnation point to the total nose-surface area. As indicated in the figure, the concave and flat-face nose configurations have approximately the same total heat input, which is 70 percent of that for a hemisphere.

CONCLUSIONS

The data obtained from this investigation, including high-speed schlieren movies, indicate that both steady and unsteady flow fields were obtained. The unsteady flow was a nonpredictable, sporadic condition more predominant at small angles of attack and higher Mach numbers. At Mach numbers of 2.49 and 3.51 the unsteady flow occurred through angles of attack of 7.5°, and at a Mach number of 4.44 the instability occurred throughout the angle-of-attack range of the tests (0° to 15°).

For steady-flow conditions the local pressures from the stagnation point of the concave nose to approximately 80 percent of the nose surface length corresponded to the total pressure behind a normal shock throughout a Mach number range from 2.49 to 4.44 and angle-of-attack range from 0° to 15°.

The stagnation heat-transfer coefficients on the concave nose were 20 percent of those for a hemisphere for steady-flow conditions. The

unstable heat-transfer coefficient at the center of the front face was approximately six times the stable value.

For steady-flow conditions and with the assumption of a constant temperature potential, the total heat input to the nose surface area was approximately the same for a concave and a flat-face nose at a Mach number of 3.51, Reynolds number of 1.0×10^6, and angle of attack of 0°, and this value was about 70 percent of that for a hemisphere.

Langley Research Center,
National Aeronautics and Space Administration,
Langley Field, Va., July 17, 1959.

L
3
5
4

REFERENCES

1. Burbank, Paige B., and Stallings, Robert L., Jr.: Heat-Transfer and Pressure Measurements on a Flat-Face Cylinder at a Mach Number Range of 2.49 to 4.44. NASA TM X-19, 1959.

2. Markley, J. Thomas: Heat Transfer and Pressure Measurement on a 5-Inch Hemispherical Concave Nose at a Mach Number of 2.0. NACA RM L58C14a, 1958.

3. Cooper, Morton, Beckwith, Ivan E., Jones, Jim J., and Gallagher, James J.: Heat-Transfer Measurements on a Concave Hemispherical Nose Shape With Unsteady-Flow Effects at Mach Numbers of 1.98 and 4.95. NACA RM L58D25a, 1958.

4. Anon.: Manual for Users of the Unitary Plan Wind Tunnel Facilities of the National Advisory Committee for Aeronautics. NACA, 1956.

5. Burbank, Paige B., and Hodge, B. Leon: Distribution of Heat Transfer on a 10° Cone at Angles of Attack From 0° to 15° for Mach Numbers of 2.49 to 4.65 and a Solution to the Heat-Transfer Equation That Permits Complete Machine Calculations. NASA MEMO 6-4-59L, 1959.

6. Lees, Lester: Laminar Heat Transfer Over Blunt-Nosed Bodies at Hypersonic Flight Speeds. Jet Propulsion, vol. 26, no. 4, Apr. 1956, pp. 259-269.

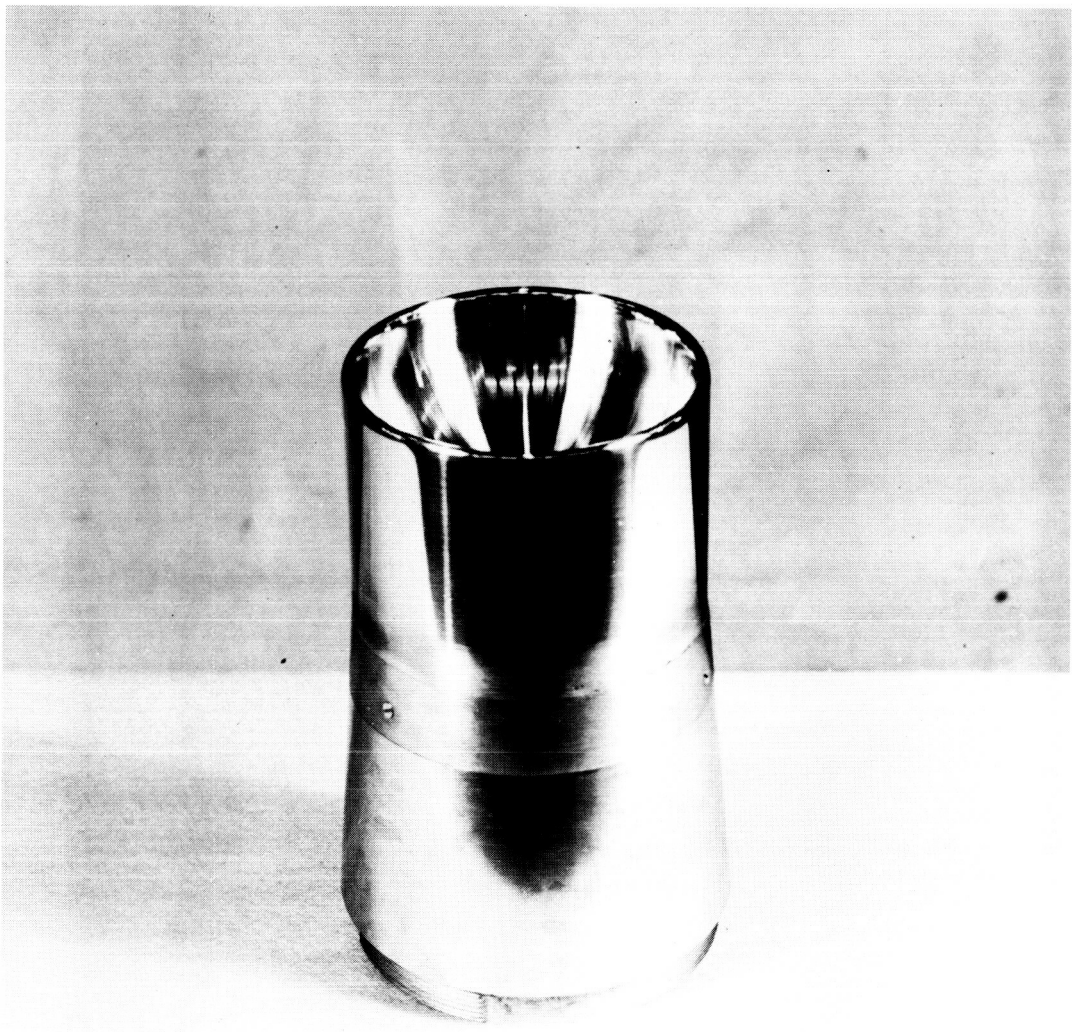

Figure 1.- Concave-nose heat-transfer and pressure model. L-59-620

Thermocouple number	$\frac{S}{S_1}$		Pressure-orifice number	$\frac{S}{S_1}$
1	0	.038	1	0
2	.18	.038	2	.33
3	.33	.039	3	.66
4	.50	.045	4	1.00
5	.66	.043	5	1.19
6	.83	.049	6	1.38
7	.95	.053	7	1.57
8	1.00	.061	8	1.00
9	1.05	.050	9	1.00
10	1.24	.050	10	1.00
11	1.43	.053	11	1.00
12	1.62	.052		
13	1.81	.052		
14	1.00	.061		
15	1.00	.061		

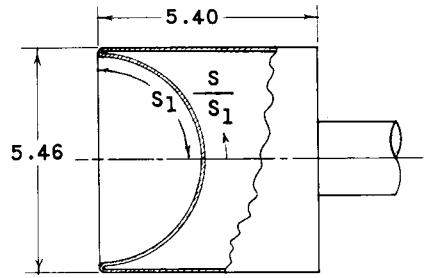

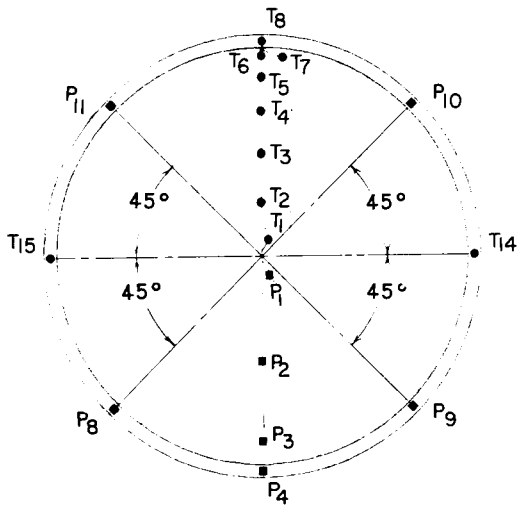

Flow

Outside radius of lip = .10
Inside radius of lip = .05
● Thermocouples
■ Pressure orifices

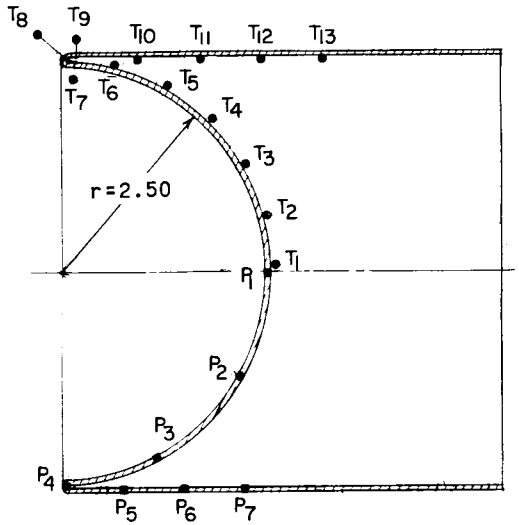

Figure 2.- Thermocouple and pressure-orifice locations. All dimensions are in inches.

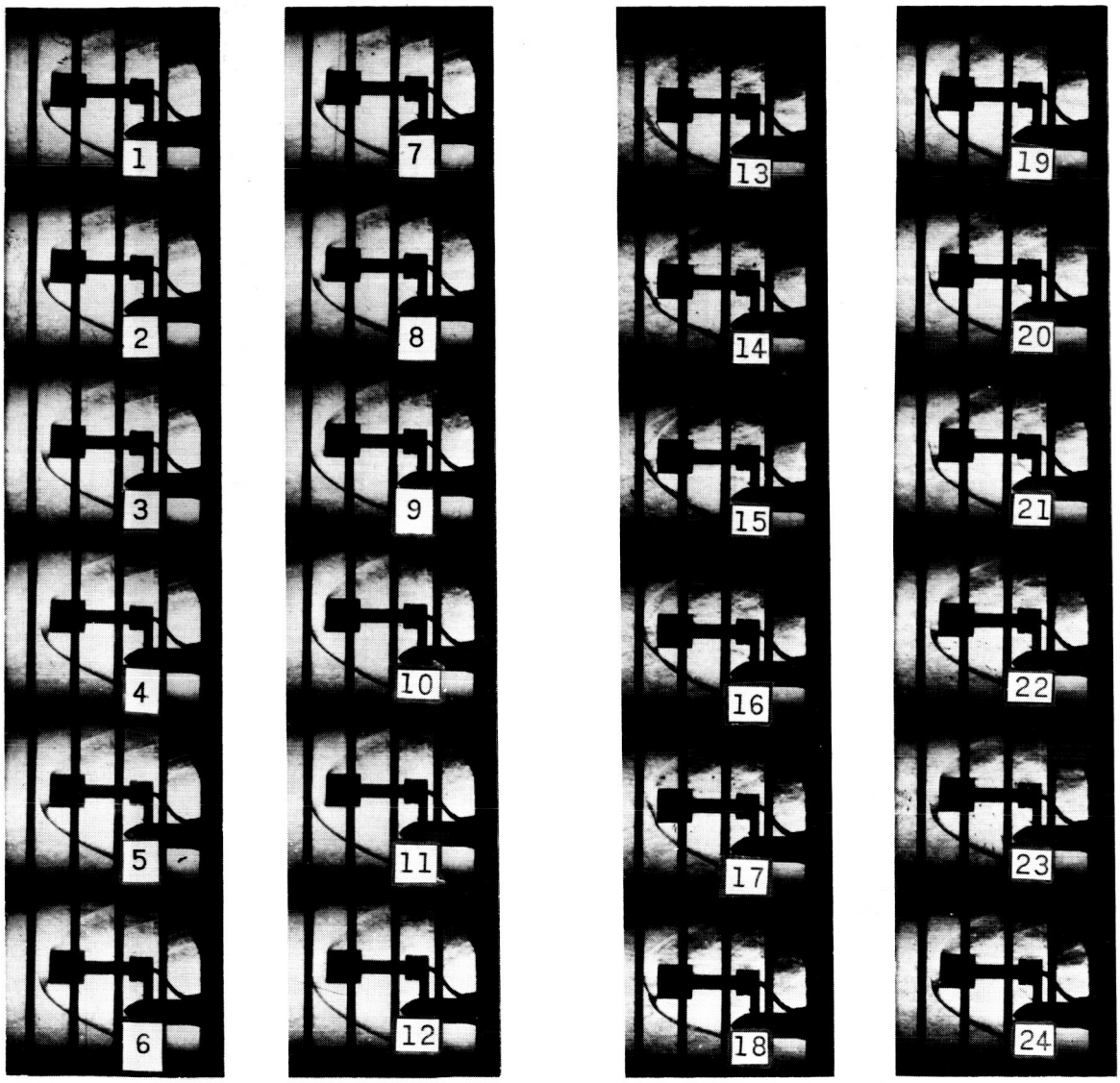

L-59-3097

Figure 3.- High-speed schlieren motion pictures of the unsteady-flow phenomenon. $M = 4.44$; $R = 1.13 \times 10^6$; $\alpha = 2^\circ$.

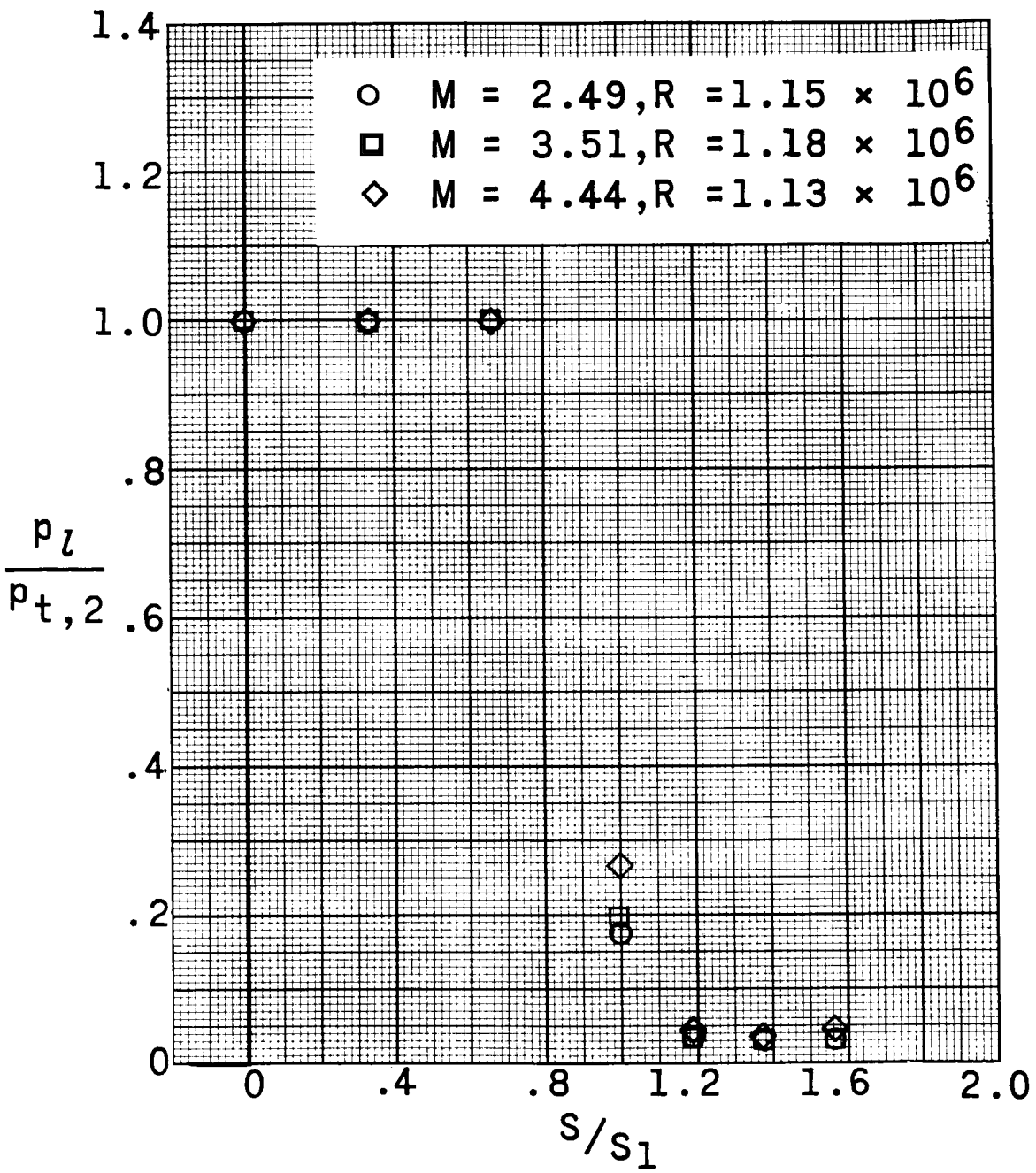

Figure 4.- Effect of Mach number on the pressure distribution over the front face and sides of concave-nose configuration. $\alpha = 0^{\circ}$.

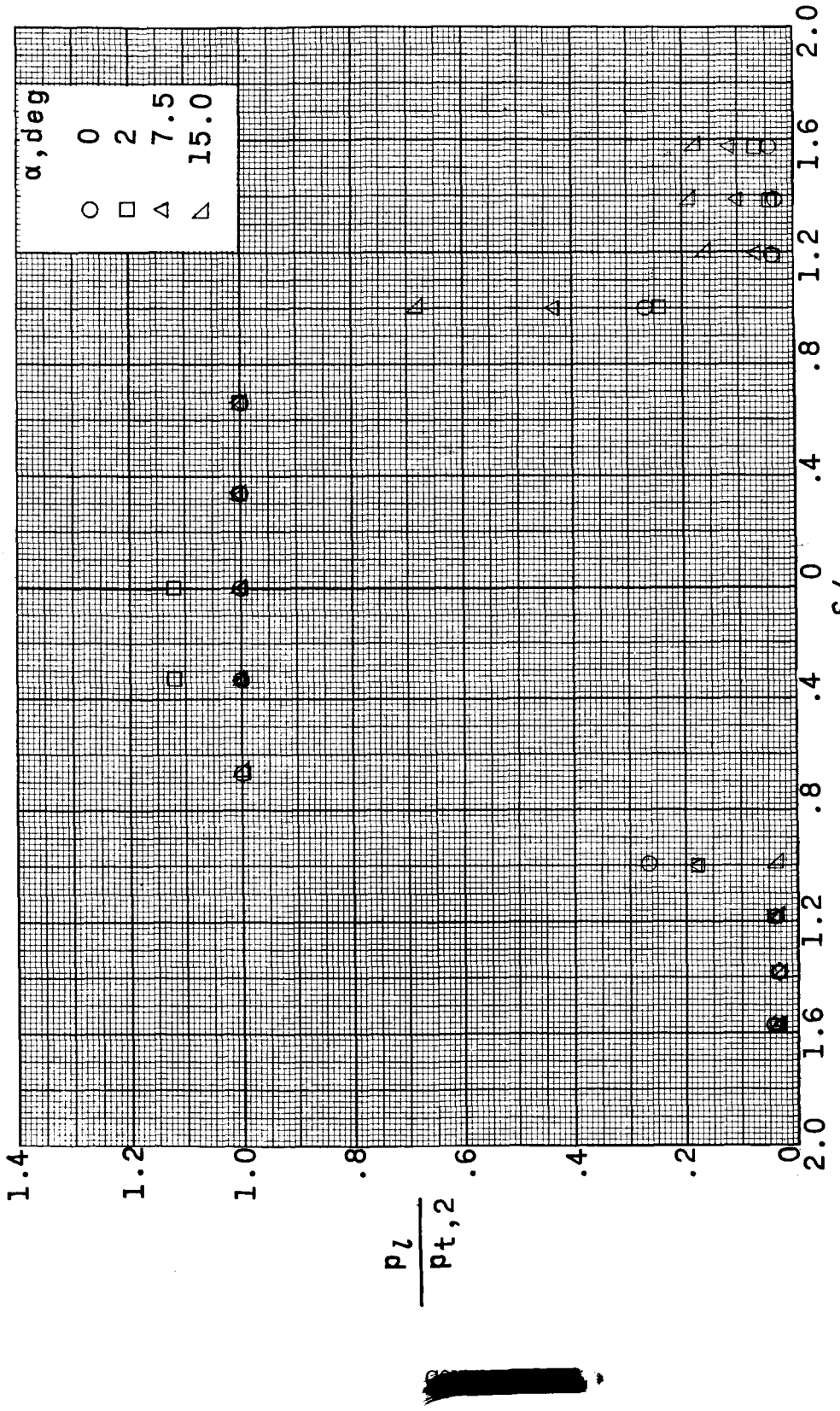

Figure 5.- Effect of angle of attack on the pressure distribution over the front face and sides of concave-nose configuration. $M = 4.44$; $R = 1.13 \times 10^6$.

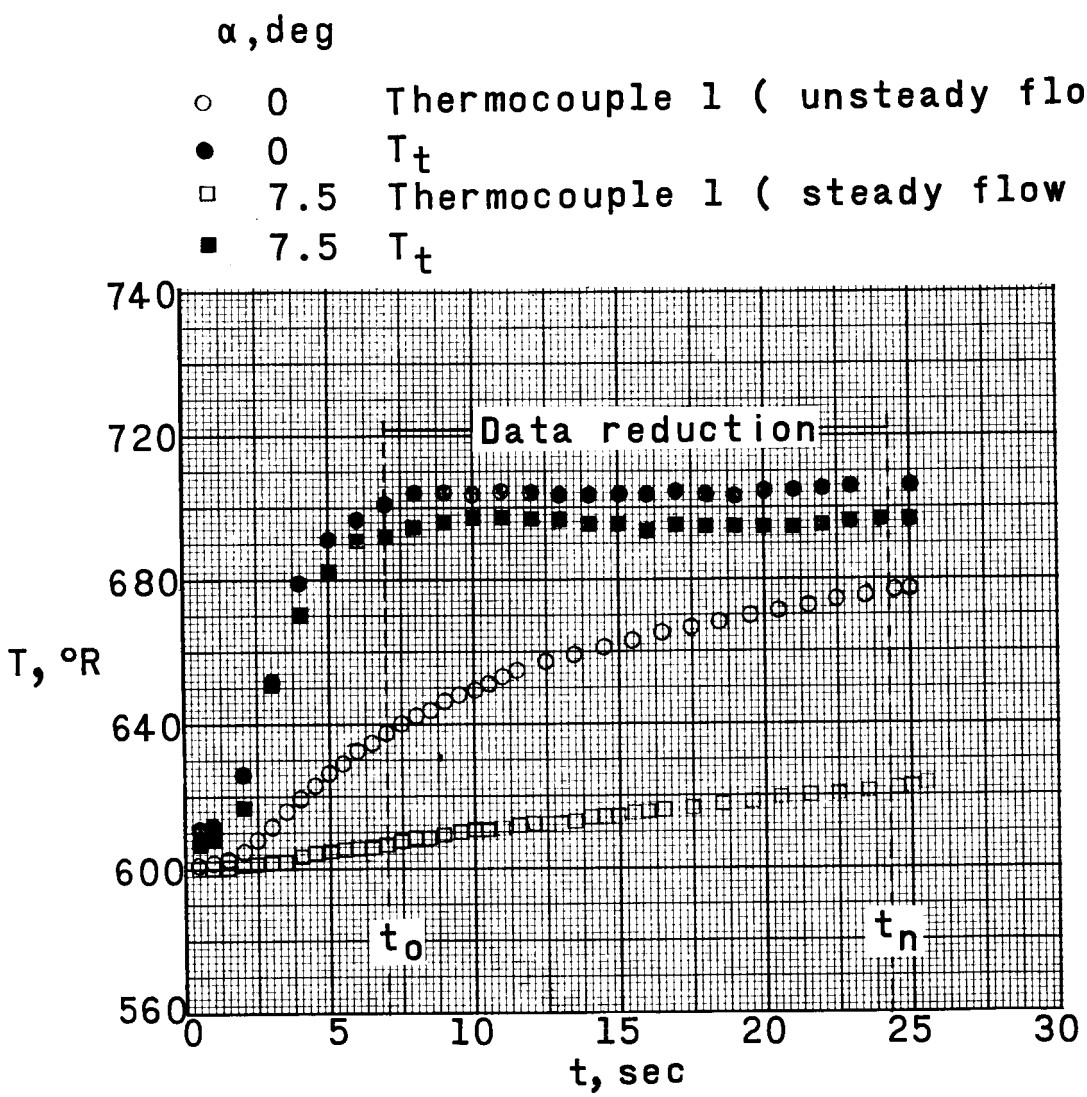

Figure 6.- Typical wall-temperature variations with time for a steady- and unsteady-flow condition. M = 2.49; R = 1.01×10^6.

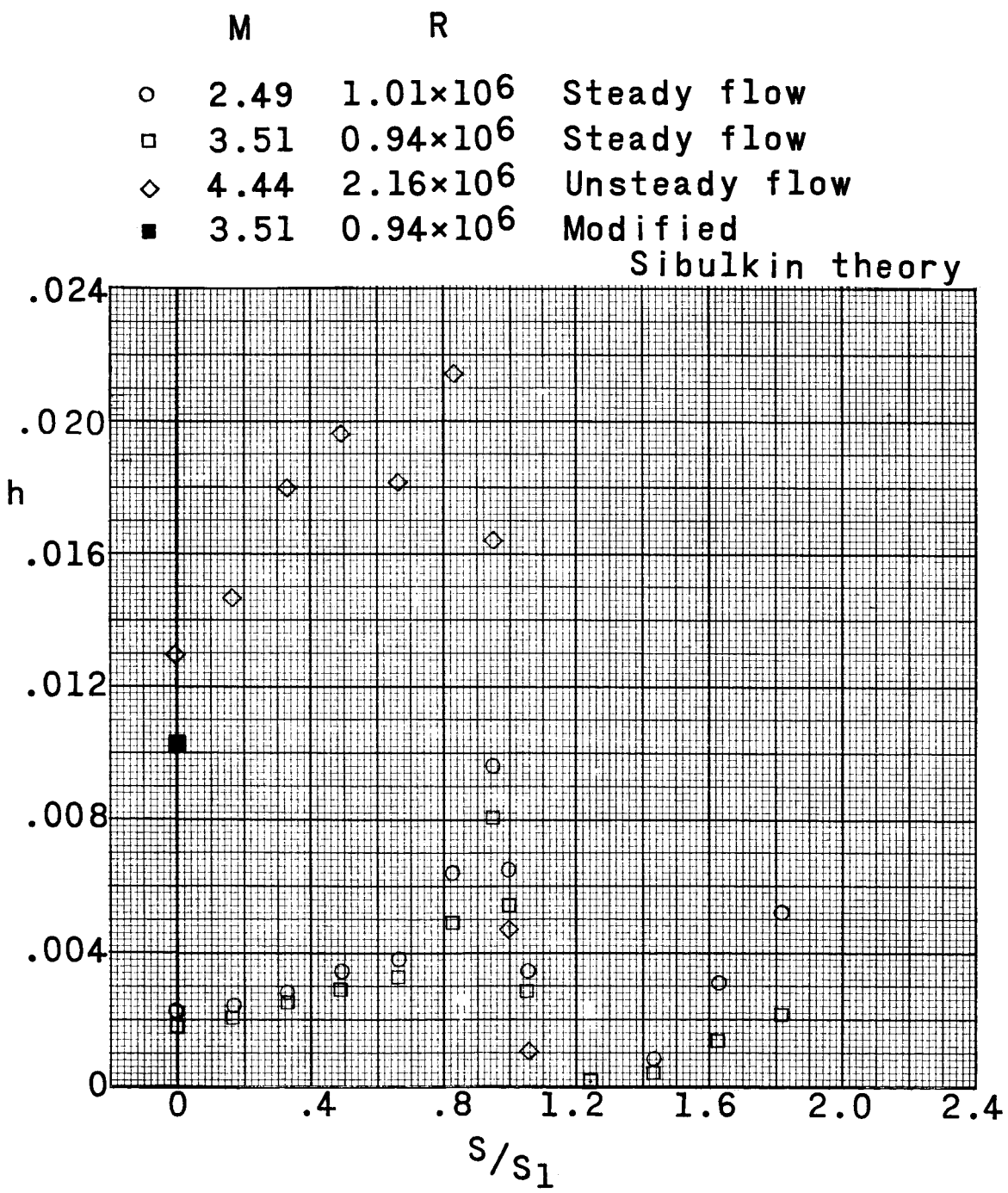

Figure 7.- Effect of Mach number on heat-transfer distribution on front face and sides of model. $\alpha = 0^{\circ}$.

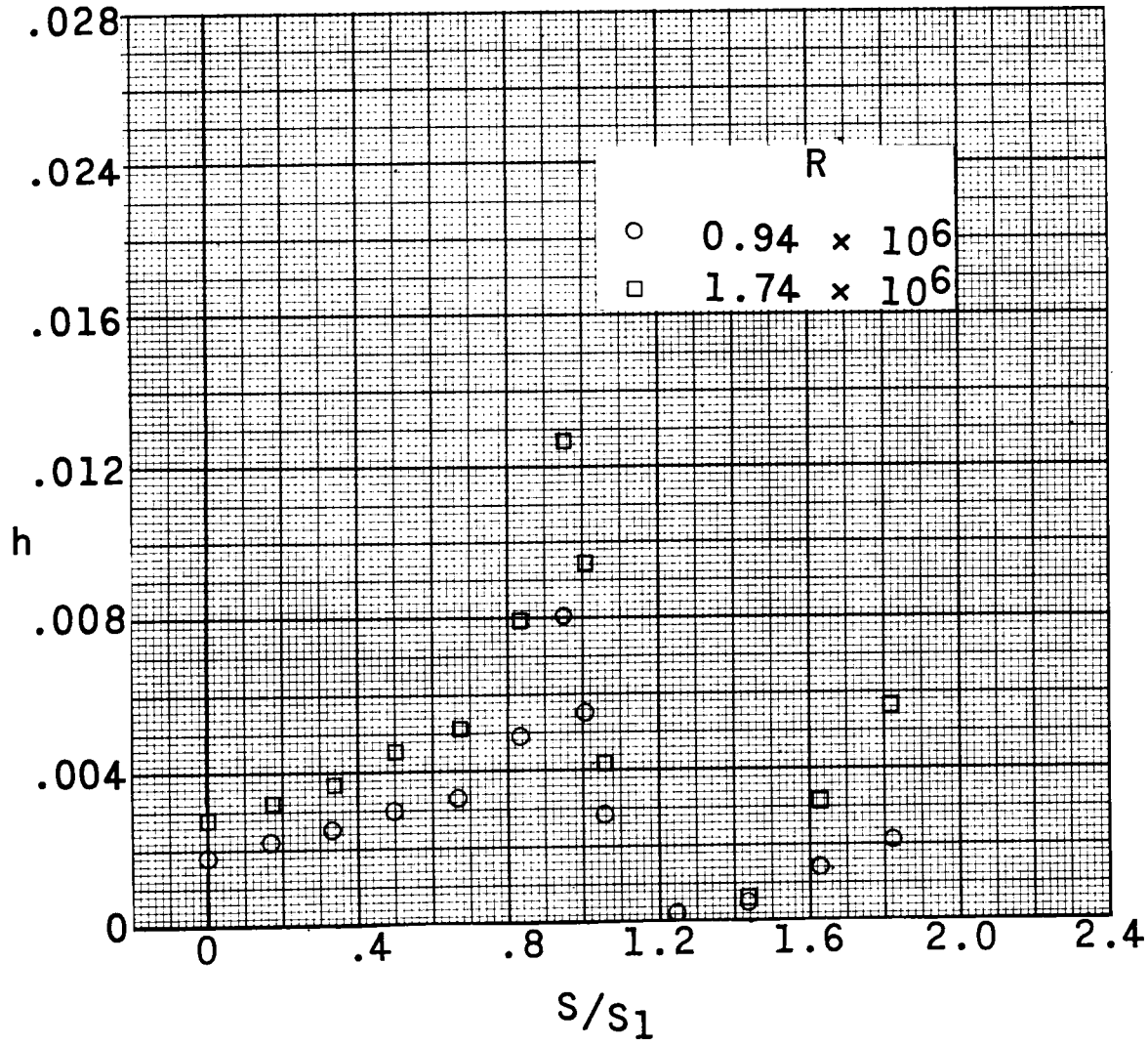

Figure 8.- Effect of Reynolds number on heat-transfer distribution on front face and sides of model. $M = 3.51$; $\alpha = 0^{\circ}$.

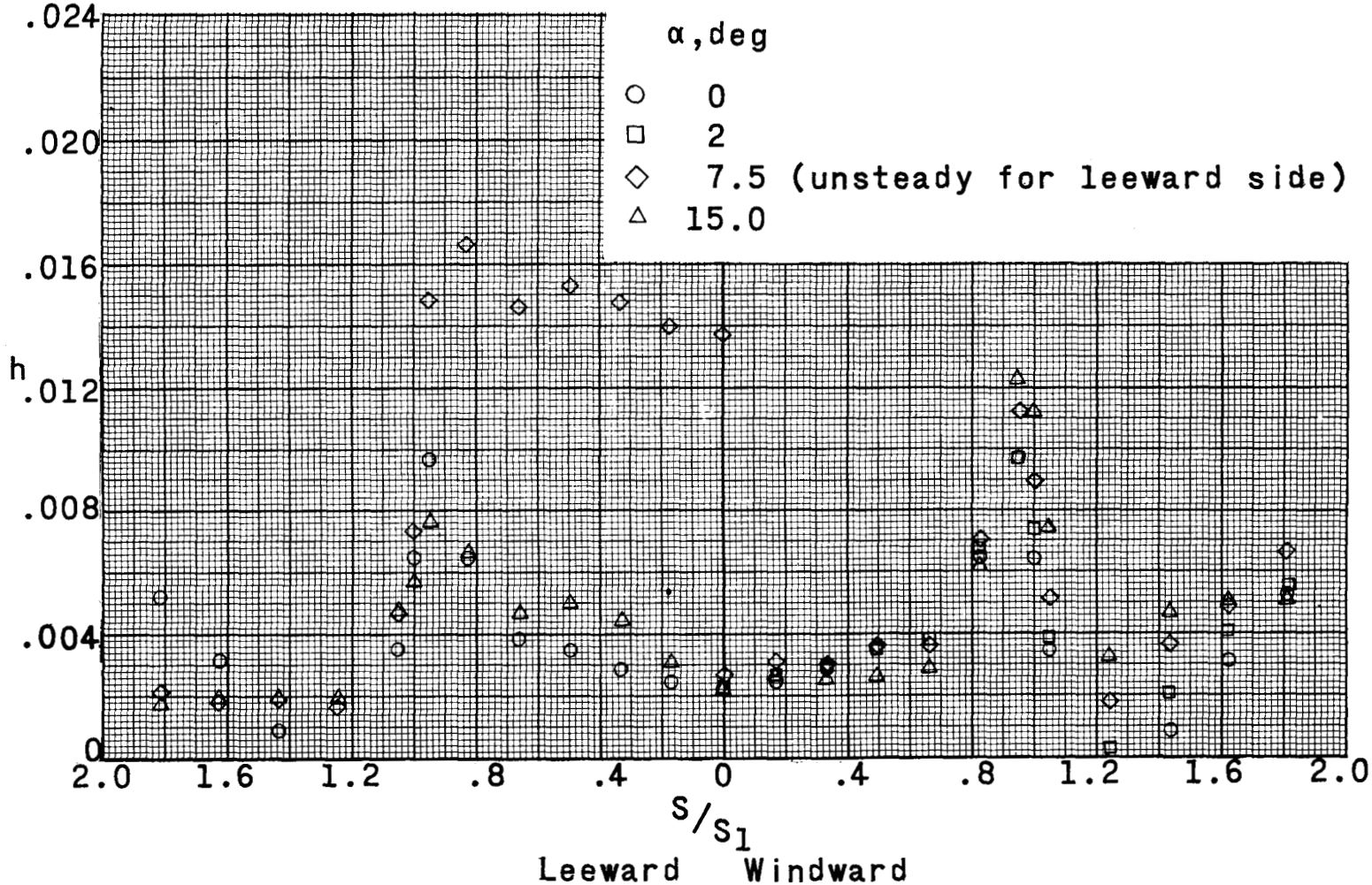

Figure 9.- Effect of angle of attack on the heat-transfer distribution over the front face and sides of model. M = 2.49; R = 1.01×10^6.

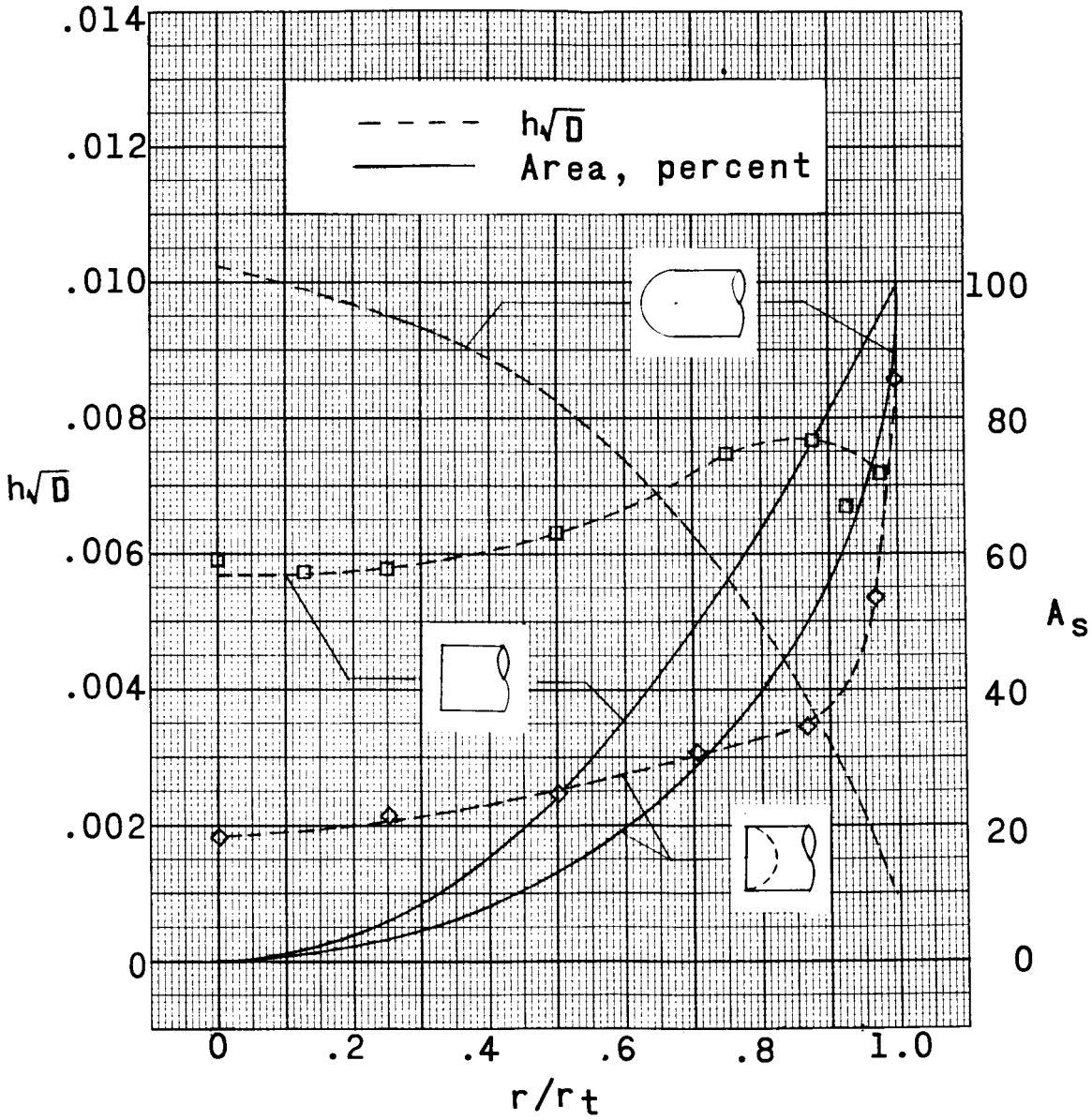

Figure 10.- The heat-transfer coefficient and area distribution for three nose configurations. M = 3.51; R = 1.8×10^6.

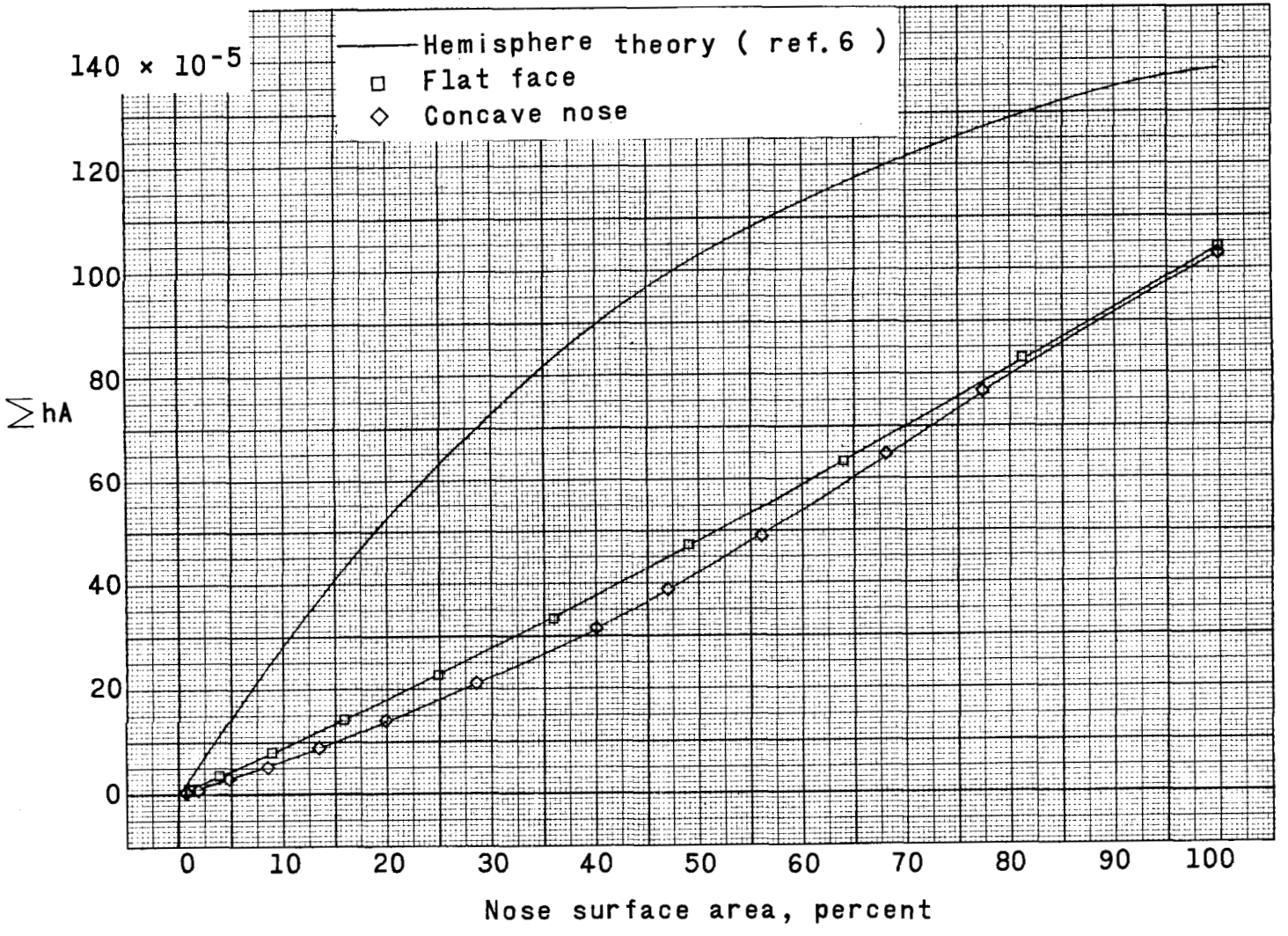

Figure 11.- Comparison of area-weighted heat-transfer coefficients for three nose configurations. $M = 3.51$; $R = 1.8 \times 10^6$.